This paper was recommended for publication in revised form by Regional Editor Lian-Ping Wang

A NEW SOLAR FUELS REACTOR USING A LIQUID METAL HEAT TRANSFER FLUID: MODELING AND SENSITIVITY ANALYSIS

Cansheng Yuan
School of Chemical & Biomolecular Engineering, Georgia Institute of Technology, Atlanta GA, U.S.A. The George W. Woodruff School of Mechanical Engineering, Georgia Institute of Technology, Atlanta GA, U.S.A.

Colby Jarrett
The George W. Woodruff School of Mechanical Engineering, Georgia Institute of Technology, Atlanta GA, U.S.A.

William Chueh
Department of Material Science and Engineering, Stanford University, Stanford CA, U.S.A.

*Yoshiaki Kawajiri
School of Chemical & Biomolecular Engineering, Georgia Institute of Technology, Atlanta GA, U.S.A.

Asegun Henry
The George W. Woodruff School of Mechanical Engineering, Georgia Institute of Technology, Atlanta GA, U.S.A. School of Materials Science and Engineering, Georgia Institute of Technology, Atlanta GA, U.S.A.

Keywords: Solar Fuels, Solar Thermochemical Reactor, Liquid Metal, Reactor Optimization, Partial Redox Cycles, Water Splitting
* Corresponding author:, Phone: (404) 894-2856, Fax: (404) 894-2866
*E-mail address: ykawajiri@chbe.gatech.edu*

ABSTRACT

A numerical model is developed to analyze a new solar thermochemical reactor using liquid metal as a heat transfer fluid. Reaction kinetics for both reduction and oxidation in two-step redox cycles using a metal oxide are modeled by fitting to experimental data. The transient model includes the heat and mass transfer and reaction kinetics for an analysis of the efficiency and to elucidate limiting factors. The reactor can achieve an efficiency of 20% for the conversion of thermal to chemical energy for our base design. For this design, the removal of oxygen during the reduction step was determined to be the bottleneck to achieve a higher efficiency. In a sensitivity analysis, the optimal reaction temperature can be found considering the trade-off between fast reaction kinetics and materials compatibility.
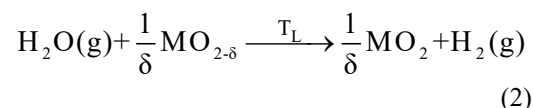
INTRODUCTION

The idea of using solar energy as high temperature process heat to make fuel has been around for more than three decades.[1–5] This idea has gained increased attention over the last few years as interest has shifted to two-step partial redox cycles.[6–24] A well-known example is the production of hydrogen fuel from water through two-step partial redox cycles using metal oxides that undergo the following two reactions:

Step 1: Reduction Reaction

$$\frac{1}{\delta}\mathrm{MO_2} \xrightarrow{T_H} \frac{1}{\delta}\mathrm{MO_{2-\delta}} + \frac{1}{2}\mathrm{O_2(g)}$$

(1)
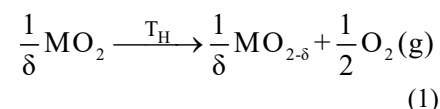
Step 2: Oxidation Reaction

$$\mathrm{H_2O(g)} + \frac{1}{\delta}\mathrm{MO_{2-\delta}} \xrightarrow{T_L} \frac{1}{\delta}\mathrm{MO_2} + \mathrm{H_2(g)}$$

(2)

In these reactions, the solid phase metal oxide serves as an oxygen storage material (OSM), denoted as MO_2. In Step 1, the OSM is heated to a high temperature T_H (e.g. 1200-1500 °C) and is subject to a low oxygen pressure (p_{O_2}) environment where it endothermically releases oxygen from its lattice. The heat required to break the chemical bonds is supplied by the high temperature solar process heat and the oxygen release is driven by the entropy increase experienced by the O_2 molecules upon liberation. This can be seen from the change in Gibbs free energy for the reaction $\Delta G = \Delta H - T\Delta S$ where ΔH represents the strength of the metal oxygen bonds, and at sufficiently high temperatures $T\Delta S$ can become greater than ΔH prompting the oxygen release. This step is followed by Step 2, where the OSM in a reduced state $MO_{2\text{-}\delta}$ and is cooled to a lower temperature T_L (e.g. 500-800°C), such that the thermodynamic driving force is reversed. In this second reaction, the OSM consumes the oxygen in H_2O to refill its oxygen vacancies, as the metal oxygen bond strength now dominates ΔG at lower temperatures. This reaction liberates hydrogen, thereby producing fuel. After Step 2, the OSM can be reheated and cycled through these two reaction steps without consuming the OSM.

Many metal oxides can be used as an OSM, and they can be divided into two categories, volatile and non-volatile materials.[25] Separation of the volatile product to avoid recombination of the products results in the low efficiency of splitting water for volatile OSMs;[26] therefore, more efforts have been devoted to research on non-volatile materials, such as Fe_3O_4, and CeO_2.[7,9]

Many solar reactor concepts have been proposed to produce fuel with this two-step water splitting process. For example, Roeb et al. built a reactor which where the OSM served as the receiver and was coated on honeycomb absorbers.[27] In their design, two identical receiver-reactors were constructed such that a quasi-continuous operation of the two-step water splitting cycle is feasible. Kaneko et al. built a rotary-type solar reactor using Ni-Mn ferrites and ceria as the OSM.[28] Muhich et al. developed a solar reactor using counter-rotating rings where OSM is coated on the surfaces.[19] In this design, the rings rotate between high temperature reduction zone and low temperature oxidation zone to enable better heat recuperation and continuous fuel production. This design allows recuperating the sensible heat in the high temperature part of the reactor via radiation, and simulations indicate a recuperative efficiency > 50%.[15,16] Gokon et al. proposed a windowed reactor, using an internally circulating fluidized bed for the thermal reduction of NiFe2O4/m-ZrO2 particles and demonstrated the concept with a laboratory scale reactor.[29] Perkins et al. tested an aerosol reactor for the dissociation of ZnO(s) to Zn(g).[26] Scheffe et al.

also used an aerosol reactor to carry out thermal reduction of ceria.[30] Koepf et al. used an inverted conical-shaped cavity where the reactant powder ZnO descends continuously as a moving bed to produce hydrogen.[31]

Despite these various efforts, the efficiency of these reactors is far below 20%, which has been cited as the efficiency regime where such processes can become economically viable at scale.[32] The largest efficiency reported in the literature is an average of 1.73% with the peak of 3.53%.[12] This is in contrast to thermodynamic analyses that suggest much higher efficiencies of over 50% are possible.[33] The key discrepancy between these thermodynamic models and reality is that they do not account for chemical reaction kinetics nor the inherent limitations on heat and mass transport. Several studies[13,16] that have constructed more comprehensive models that consider transport kinetics, have agreed with experiments and shown why the reactors are extremely inefficient – predicting efficiencies on the order of 1%. The conclusions of these models has been that most of the incident sunlight is simply re-emitted as thermal radiation after being absorbed at such high temperatures on the walls of the cavity.[13] In such designs the cavity walls serve two purposes and facilitate two forms of energy conversion, namely as the receiver which converts the sunlight to heat via optical absorption and as the reactor which converts the thermal energy to energy stored in the chemical bonds of the reaction products.

Recently we have introduced a new concept for the reactor design, which separates the receiver and reactor into two separate devices to reach higher efficiency.[34] In our analysis, we considered two efficiencies, one for solar to thermal energy ($\eta_{\text{solar-thermal}}$) and another for thermal to chemical energy ($\eta_{\text{thermal-chemical}}$), thus expressing the overall efficiency $\eta_{\text{solar-chemical}}$ as the product of these two efficiencies, via $\eta_{\text{solar-chemical}} = \eta_{\text{solar-thermal}}\eta_{\text{thermal-chemical}}$. We proposed a new concept that separates the two conversions steps: solar to thermal, and thermal to chemical. The first energy conversion, solar to thermal, is carried out by a receiver. The second energy conversion, thermal to chemical, is performed by a reactor which can be designed and operated separately. To achieve a high overall efficiency, it is crucial to optimize the reactor.

In this study, we model the reactor and carry out an analysis to optimize the design and operation. Based on the reactor designed, we have constructed a model that has fully incorporated chemical reaction kinetics, heat and mass transfer inside the reactor, which is rare except the work from Keene et al.[13] We carry out a detailed study on the reactor concept to estimate the efficiency of this reactor design and identify its limitations. A sensitivity analysis is performed to optimize the reactor design and operating parameters. Since the main focus of this paper is to show the modelling of a new reactor concept,

the reactor and its operation will be introduced only briefly here, but is discussed in more detail elsewhere[34].

NEW REACTOR DESIGN

In our new concept, two separate devices are used, a solar receiver which handles the solar-thermal conversion, and a thermal-chemical reactor which converts the thermal energy to fuel energy. Each of these two devices can be designed and optimized separately to achieve a higher efficiency. These two devices are connected through a high temperature liquid metal (LM) which serves as a heat transfer fluid. This concept is schematically illustrated in Figure 1. In this scheme, the overall conversion of solar energy to chemical energy to be stored in hydrogen fuel is divided into two parts: solar to thermal, and thermal to chemical (fuel). The efficiency of the former conversion is $\eta_{\text{solar-thermal}}$, while that of the latter is $\eta_{\text{thermal-chemical}}$. In DeAngelis et al,[35] a solar receiver that uses a LM has been shown to facilitate the solar-thermal conversion at a high efficiency ($\eta_{\text{solar-thermal}} \sim$ 80-90%). In this study, we investigate a reactor system that achieves a high value of $\eta_{\text{thermal-chemcial}}$ allowing for a high overall efficiency $\eta_{\text{solar-chemical}} = \eta_{\text{solar-thermal}}\eta_{\text{thermal-chemical}}$.
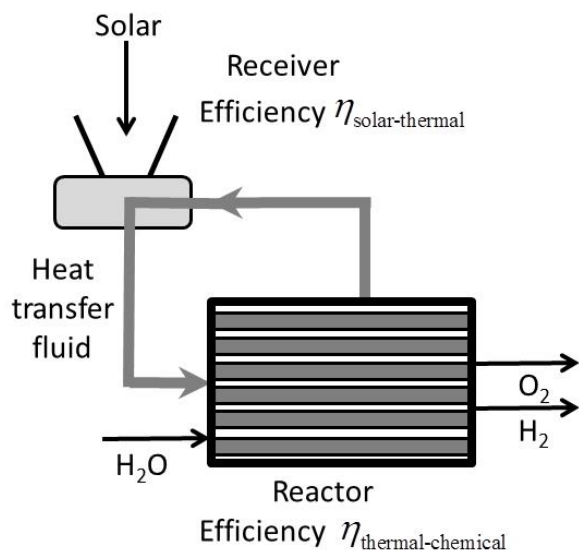

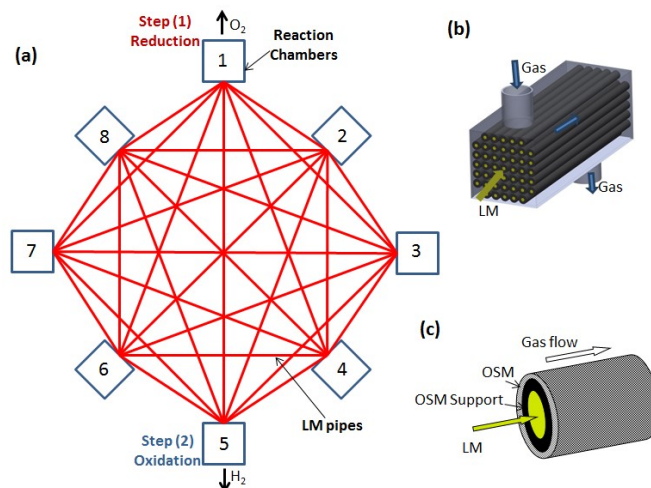Figure 1 New receiver-reactor design concept with two separate devices.

Figure 2 New reactor design concept using LM. (a) Thermochemical reactor schematic showing an array of sealed reaction chambers interconnected by a piping network. The chambers are denoted by square boxes and the piping network consists of pipes that do not intersect, but are overlaid on top of each other, so that each acts as a dedicated conduit for LM circulation between a pair of chambers. (b) A schematic of an individual reaction chamber, which consists of an array of pipes carrying an LM through the inner bore. (c) A cross-section of one tube inside of the chamber.

We recently developed a new reactor design as shown in Figure 2,[34] which is discussed briefly here. It is envisioned that the LM would be tin (Sn) and the reactor would be largely constructed out of graphite. Sn melts at 232°C and does not boil until 2602°C at 1 atm, thus it would remain liquid and stable over the entire temperature range of interest. Graphite is inexpensive, easily machinable into complex shapes and is stable up to ~ 3000°C. Most importantly, graphite and Sn are fully chemically compatible at all temperatures, since they do not form any chemical compounds (e.g., no corrosion). Our design employs an array of sealed reaction chambers that are interconnected in a piping network which allows the LM to transfer heat between the chambers (see Figure 2(a)). In our system, all reaction chambers go through the two reaction steps at different times and therefore have different temperatures at any given instant. In the proposed reactor concept, the two reaction steps Eqs. (1) and (2), as well as the heat recuperation, occur cyclically and semi-continuously in separate reaction chambers. Each individual reaction chamber consists of an array of pipes (see Figure 2(b)), contained in a hermetically sealed outer housing. Each pipe serves as a containment material for the LM flowing through its inner bore (see Figure 2(b) and (c)). Each pipe also has the OSM coated around its outer diameter.
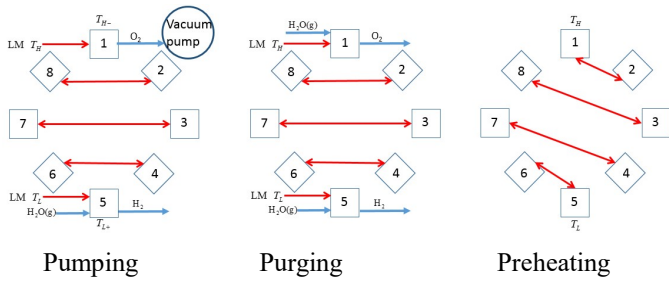
Figure 3 A schematic diagram of the reaction and heat recuperation strategy for an eight-chamber reactor system. Red lines denote which pipe channels are open and circulate the LM to exchange heat and bring different reaction chambers into equilibrium. Only the first stage is shown in this figure, while the remaining seven stages follow a similar sequence. Each stage includes three steps, pumping, purging and preheating.

The reaction and heat recuperation strategy for an eight-chamber reactor system is shown in Figure 3. While this figure shows only the first stage, one complete cycle of reaction and heat recuperation includes eight stages, where the remaining stages follow a similar sequence. Each stage has three steps, pumping, purging and preheating:

Pumping step: The first step shown in Figure 3 is the pumping step, where Chamber 1 with initial temperature T_{H-}, which is lower than T_H, is heated by the LM from the solar receiver and undergoes the reduction step (Equation (1)). In this step, a vacuum pump is used to lower the total pressure of Chamber 1 to approximately 10^{-2} atm. Simultaneously, on the opposite side of the reactor network, Chamber 5 at the initial temperature T_{L+} is cooled by LM at the temperature of T_L, and then undergoes the oxidation step (Equation (2)). Also simultaneously, the chambers in between 1 and 5 exchange thermal energy with chambers amongst themselves to recuperate heat.

Purging step: The pumping step described above is followed by the purging step, where low pressure steam is introduced to purge the oxygen in the chamber further reducing the oxygen partial pressure P_{O_2}. During this step, the heat recuperation and oxidation reaction in Chamber 5 still continue in the same way as in the pumping step.

Preheating step: Finally in the preheating step, the LM at the highest temperature T_H in Chamber 1 exchanges heat with Chamber 2 to prepare Chamber 2 for the reduction step in the next stage, while Chamber 5 exchanges heat with Chamber 6 for the reoxidation reaction.

In the next stage, the entire sequence of the pumping, purging, and preheating steps are repeated while the locations of the corresponding chambers rotate clockwise; i.e. Chamber 2 undergoes the reduction step and Chamber 6 performs the oxidation step. The entire sequence of the pumping, purging and preheating steps are repeated in a cyclic manner without having to physically move any of the chambers. As a result, the cyclic operation is achieved by moving the LM heat transfer fluid instead, which allows for efficient recuperation with minimal high temperature moving parts.

MODELLING METHOD

In this section we describe the mathematical model used in our simulations. The reactor chamber can be divided into four layers: the bulk gas, OSM, OSM support, and LM. Our model consists of mass and energy balance equations for all these layers as well as the reaction kinetics. One of the main assumptions in our model is that the behavior of each pipe can be described by that of a single pipe. Under this assumption our model simulates only one single pipe inside of the reactor, as shown in Figure 4 (a), to estimate the performance of the entire chamber. All extensive variables such as flow rates and energy expenditures are multiplied by the total number of pipes in a reaction chamber. This assumption is valid if the gas and LM are distributed equally to all pipes[36], which can be realized by carefully designing the distributor at the gas inlet and collector at the gas outlet.[37] Flow simulations of the base reactor geometry indicated that with four symmetric inlet and outlet ducts, the flow was quite uniform and only resulted in efficiency changes ~ 1%.
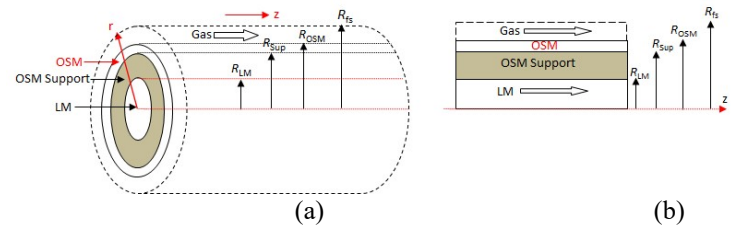

(a) (b)

Figure 4 (a) four layers of one tube inside of the reactor chamber. (b) Two-dimensional cross-sectional view of single pipe.

MODELLING ASSUMPTIONS

To further simplify our model, the following assumptions were made for the bulk gas layer:

- The ideal gas law is valid everywhere.

- The pressure drop in the axial direction in the chamber is negligible. Our estimation using empirical correlations suggests that the pressure drop is below 10% for the range of flow rates considered in this study, and the influence of the pressure change of such

a magnitude on the heat and mass balances is negligible.

- The radial distribution of P_{O_2} within the bulk gas phase, outside the boundary layer, can be neglected. This assumes the gas temperature and concentration are functions of z and t but not R.

- Diffusion and heat conduction in the axial direction of bulk gas flow are neglected, since the gas density and thermal conductivity is low. The volume that the gas occupies around a single OSM pipe is given as free space[36], which encircles the OSM pipe. The radius of this free space is given as R_{fs} (Figure 4 (a) and (b)).

For the OSM layer, the following assumptions are made:
- The OSM layer is a porous medium which consists of OSM particles of the diameter d_{32}.

- There is no mass or thermal convective flow inside the pores of the OSM layer, because the pores are sufficiently small.

- The diffusion rate in the OSM is calculated using Chapman-Enskog theory[38], while diffusion in the OSM particle is assumed to be significantly faster, such that it presents negligible impedence[9,13].

- Mass transfer between the OSM layer and the OSM support layer is neglected; i.e. the OSM support material is non-permeable to H_2 and O_2, which can be realized by a nonreactive oxide diffusion barrier layer to block the gas penetration.

For the LM layer, the following assumptions are made:
- The radial temperature distribution of the LM can be ignored; i.e. the LM temperature is a function of z and t but not R.

The last assumption is justified by the high thermal conductivity of the LM, as fully developed laminar flow in a pipe gives $Nu_{LM} = 4.64$.[39] This high Nusselt number leads to a heat transfer coefficient of approximately 12,000 W m^{-2} K^{-1}. The thermal resistance of LM with such a high conductivity is negligible compared to the conductive resistance of the OSM layer, which has thermal conductivities of only up to 1.0 W m^{-1} K^{-1}, and thicknesses of 3 mm respectively. Under these assumptions, the simulation of one single pipe can be modeled in a two dimensional spatial domain as shown in Figure 4(b).

ENERGY BALANCE EQUATIONS

The heat transfer between the OSM and LM can be characterized by the heat transfer coefficient h_{LM} (computed from Nu_{LM}), such that the energy balance equation across the boundary between the LM and OSM support can be written as

$$\rho_{LM} C_P^{LM} \frac{\partial T_{LM}}{\partial t} + \rho_{LM} C_P^{LM} u_{LM} \frac{\partial T_{LM}}{\partial z} - \lambda_{LM} \frac{\partial^2 T_{LM}}{\partial z^2} = A_{LM} h_{LM} \left(T_{Sup}(R_{Sup}, z, \right.$$
(3)

where A_{LM} is the surface area of the pipe normalized by the volume (e.g., 4/D). Correlations from Sharafat and Ghoniem[40] were used to describe the temperature dependent properties (e.g., ρ_{LM}, C_P^{LM} and λ_{LM}) of the LM, which is assumed to be tin (Sn). The average temperature of the LM over the z direction is used in the correlation as the representative fluid temperature. The heat transfer coefficient h_{LM} is then computed as:[39]

$$Nu_{LM} = \frac{h_{LM} d_{LM}}{\lambda_{LM}} = 4.64$$
(4)

The energy balance within the OSM support layer is given by:

$$\rho_{Sup} C_p^{Sup} \frac{\partial T_{Sup}}{\partial t} - \lambda_{Sup} \left(\frac{\partial^2 T_{Sup}}{\partial R^2} + \frac{1}{R} \frac{\partial T_{Sup}}{\partial R} + \frac{\partial^2 T_{Sup}}{\partial z^2} \right) = 0$$
(5)

To obtain the temperature of the OSM the heat balance equation within the OSM phase can be written as:

$$\rho_{OSM} C_P^{OSM} \frac{\partial T_{OSM}}{\partial t} - \lambda_{OSM} \left(\frac{\partial^2 T_{OSM}}{\partial R^2} + \frac{1}{R} \frac{\partial T_{OSM}}{\partial R} + \frac{\partial^2 T_{OSM}}{\partial z^2} \right) = r_i \Delta H_i,$$

$i = \text{reduction, reoxidation}$
(6)

Here, we assume that the heat conduction in the OSM phase can be characterized by the overall thermal conductivity, λ_{OSM}, which incorporates the effects of the lower thermal conductivity of the gas filling the pore space. The right hand side of this equation is the source term due to the heat of reaction, where r_i is the production rate of oxygen or hydrogen and ΔH_i is the corresponding heat of reaction (Equation (1) and (2)).

The energy balance in bulk gas layer is given by:

$$\rho_{gas}C_P^{gas}\frac{\partial T_{gas}}{\partial t}+\rho_{gas}C_P^{gas}\frac{\partial(u_{gas}T_{gas})}{\partial z}-\lambda_{gas}\frac{\partial^2 T_{gas}}{\partial z^2}$$
$$=A_{OSM}h_{gas}\left(T_{OSM}(R_{OSM},z,t)-T_{gas}(z,t)\right)$$

(7)

The heat transfer coefficient h_{gas} is computed as:[41]

$$Nu_{gas}=\frac{h_{gas}d_{OSM}}{\lambda_{gas}}=1.845Gz_H^{1/3}$$

(8)

where:

$$Gz_H=\frac{d_{OSM}^2 u_{gas}}{\alpha_{gas}L}$$

(9)

The boundary conditions necessary to solve these set of equations are given in Table 1.

Table 1 Boundary condition to solve energy balance equations.

Location	Boundary condition
$z=0$	$T_{LM}(0)=T_{gas}(0)=T_{inlet}$
$R=R_{LM}$	$\lambda_{Sup}\frac{\partial T_{Sup}(R_{LM},z,t)}{\partial r}=h_{LM}\left(T_{Sup}(R_{LM},z,t)-T_{LM}(z,t)\right)$
$R=R_{Sup}$	$\lambda_{Sup}\frac{\partial T_{Sup}(R_{Sup},z,t)}{\partial r}=\lambda_{OSM}\frac{\partial T_{OSM}(R_{Sup},z,t)}{\partial r}$
	$T_{Sup}(R_{Sup},z,t)=T_{OSM}(R_{Sup},z,t)$
$R=R_{OSM}$	$-\lambda_{OSM}\frac{\partial T_{OSM}(R_{OSM},z,t)}{\partial r}=h_{gas}\left(T_{OSM}(R_{OSM},z,t)-T_{gas}(z,t)\right)$

where T_{inlet} is inlet temperature of LM and purge gas, which depends on the specific step of the cycle. We assume that in the reduction step, $T_{inlet}=1500\,^{O}C$, and in the oxidation operation, $T_{inlet}=800\,^{O}C$.

MASS BALANCE EQUATIONS

The O_2 or H_2 molecules produced in the OSM layer are first transferred from the surface of a ceria particle to the top of the OSM layer via diffusion. For this diffusion, the effective diffusion coefficient is represented by D_{eff}, which is discussed in detail in the supplementary information. The mass balance in the OSM layer is given by:

$$\varepsilon\frac{\partial c_{i,OSM}}{\partial t}-\varepsilon D_{eff}\left(\frac{\partial^2 c_{i,OSM}}{\partial R^2}+\frac{1}{R}\frac{\partial c_{i,OSM}}{\partial R}+\frac{\partial^2 c_{i,OSM}}{\partial z^2}\right)=-r_i$$

(10)

where ε is the porosity of OSM, r_i is the reaction rate and we used the same reaction kinetics expression in Keene et al.[13]

The gas molecules travel across the boundary layer between the bulk gas layer and OSM, where the rate is characterized by the mass transfer coefficient k_{gas}. The mass balance equation is given by:

$$\frac{\partial c_{i,gas}}{\partial t}+u_{gas}\frac{\partial c_{i,gas}}{\partial z}+c_{i,gas}\frac{\partial u_{gas}}{\partial z}+k_{gas}A_{OSM}\varepsilon\left(c_{i,gas}(z,t)-c_{i,OSM}(R_{OSM},z,t)\right)=$$

(11)

where A_{OSM} is the surface area per unit volume of the OSM layer, given by $A_{OSM}=\dfrac{R_{fs}}{R_{fs}^2-R_{OSM}^2}$.

The gas velocity u_{gas} is obtained from the summation of the mass balance equations for all species:

$$\frac{\partial c_{Total}}{\partial t}+u_{gas}\frac{\partial c_{Total}}{\partial z}+c_{Total}\frac{\partial u_{gas}}{\partial z}+\sum k_{gas}A_{OSM}\varepsilon\left(c_{i,gas}(z,t)-c_{i,OSM}(\right.$$

(12)

The boundary conditions between OSM layer and bulk gas for the mass balance are:

$$D_{eff}\frac{\partial c_{i,OSM}(R_{OSM},z,t)}{\partial R}=k_g(c_{i,gas}(z,t)-c_{i,OSM}(R_{OSM},z,t))$$

(13)

This equation is solved with the inlet boundary condition of bulk gas layer, $c_{i,gas}(0,t)=c_{i,gas,in}$.

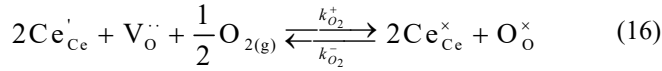The mass transfer coefficients k_{gas} can be computed as[42]

$$Sh=\frac{k_{gas}d_{OSM}}{D_{gas}}=1.2824(Re_{gas}\,Sc_{gas}\,\frac{d_{OSM}}{L})^{1.079}$$

(14)

Here, Sc_{gas} is given by

$$Sc_{gas}=\frac{\mu_{gas}}{\rho_{gas}D_{gas}}$$

(15)

REACTION KINETICS

For the reduction reaction, Eq. (1) can be rewritten using Kroger Vink notation as follows:[9]

$$2\,Ce'_{Ce} + V_O^{\cdot\cdot} + \frac{1}{2}O_{2(g)} \underset{k_{O_2}^-}{\overset{k_{O_2}^+}{\rightleftarrows}} 2\,Ce_{Ce}^\times + O_O^\times \qquad (16)$$

The oxygen production rate can then be described by[13]

$$r_{O_2}(R,z,t) = \frac{k_{O_2}^+}{2}\left\{ \frac{(1-2\delta)^2(1-0.5\delta)}{2K_{KV}} - \left(\frac{p_{O_2}(R,z,t)}{p_{ref}}\right)^{\frac{1}{2}}\delta^3 \right\} \qquad (17)$$

The reaction rate constant $k_{O_2}^+$ is given by

$$k_{O_2}^+ = k_{O_2}A_R = k_{O_2}\frac{6(1-\varepsilon)}{d_{32}},\quad \text{where}\quad A_R \text{ is the specific}$$

surface area (i.e. surface area of particles per unit volume), and d_{32} is the particle diameter of the OSM material.

The equilibrium constant K_{KV} is computed from

$$K_{KV} = \exp\left(-\frac{\Delta\bar{h}_{KV} - T\Delta\bar{s}_{KV}}{\bar{R}T}\right) \qquad (18)$$

where $\Delta\bar{h}_{KV}$ and $\Delta\bar{s}_{KV}$ are enthalpy and entropy of the reduction reaction and are obtained from the experimental data in Panlener[43].

The partial pressure of oxygen p_{O_2} is computed from the ideal gas law:

$$p_{O_2} = c_{O_2}RT \qquad (19)$$

The nonstoichiometry $\delta(R,z,t)$ can be computed from the following equation:[13]

$$\frac{\partial}{\partial t}\left\{\frac{\rho_{MO_2}}{M_{MO_2}}(1-\varepsilon)\delta(R,z,t)\right\}$$
$$= k_{O_2}^+\left\{ \frac{(1-2\delta(R,z,t))^2(1-0.5\delta(R,z,t))}{2K_{KV}} - \left(\frac{p_{O_2}(R,z,t)}{p_{ref}}\right)^{\frac{1}{2}}\delta(R,z,t)^3 \right\} \qquad (20)$$

In this reaction rate model, the reaction rate constant k_{O_2} is obtained by fitting Eq. (17) to experimental data. For the oxidation reaction, the reaction rate of hydrogen production can be described by[6]

$$r_{H_2}(R,z,t) = \frac{k_{H_2}^+}{2}\delta^m(R,z,t)\left(\frac{p_{H_2O}(R,z,t)}{p_{ref}}\right)^{0.54} \qquad (21)$$

In a similar manner to $k_{O_2}^+$, the reaction rate constant for the oxidation reaction $k_{H_2}^+$ is given by

$$k_{H_2}^+ = k_{H_2}A_R = k_{H_2}\frac{6(1-\varepsilon)}{d_{32}}.$$

The change of nonstoichiometry can be given by

$$\frac{\partial}{\partial t}\left\{\frac{\rho_{MO_2}}{M_{MO_2}}(1-\varepsilon)\delta(R,z,t)\right\} = k_{H_2}^+\delta^m(R,z,t)\left(\frac{p_{H_2O}(R,z,t)}{p_{ref}}\right)^{0.5} \qquad (22)$$

In this reaction rate model, the reaction rate constant $k_{H_2}^+$ and reaction order m must be obtained from experimental data as described in the following section.

KINETIC PARAMETER ESTIMATION

The equilibrium constant K_{KV} can be modeled by the following equation:[9]

$$K_{KV} = \frac{[Ce_{Ce}^\times]^2[O_O^\times]}{\left(\frac{p_{O_2}(R,z,t)}{p_{ref}}\right)^{1/2}[Ce'_{Ce}]^2[V_O^{\cdot\cdot}]} \qquad (23)$$
$$= \frac{(1-2\delta_{eq})^2(1-0.5\delta_{eq})}{\left(\frac{p_{O_2}(R,z,t)}{p_{ref}}\right)^{1/2}\delta_{eq}^3}$$

where δ_{eq} is the equilibrium nonstoichiometry. The experiment reported by Panlener, et al. [43] provides the data necessary to obtain $\Delta\bar{h}_{KV}$ and $\Delta\bar{s}_{KV}$. From the oxygen partial pressure and nonstoichiometry at equilibrium, as shown in Figure 5 one can obtain the plot of $\log(K_{KV})$ vs $1/T$, from which $\Delta\bar{h}_{KV}$ and $\Delta\bar{s}_{KV}$ can be computed. From this plot, we can

carry out a regression analysis for $\Delta \bar{h}_{KV}$ and $\Delta \bar{s}_{KV}$ as a function of δ_{eq}. We obtain quadratic approximations as follows:

$$\Delta \bar{h}_{KV} = -7.904 \times 10^6 \, \delta_{eq}^2 + 1.56 \times 10^6 \, \delta_{eq} - 4.825 \times 10^5 \quad (24)$$

$$\Delta \bar{s}_{KV} = -322.6 \, \delta_{eq}^2 + 304.5 \, \delta_{eq} - 144.1 \quad (25)$$

where unit of $\Delta \bar{h}_{KV}$ and $\Delta \bar{s}_{KV}$ are in kJ/mol and kJ/mol K, respectively.
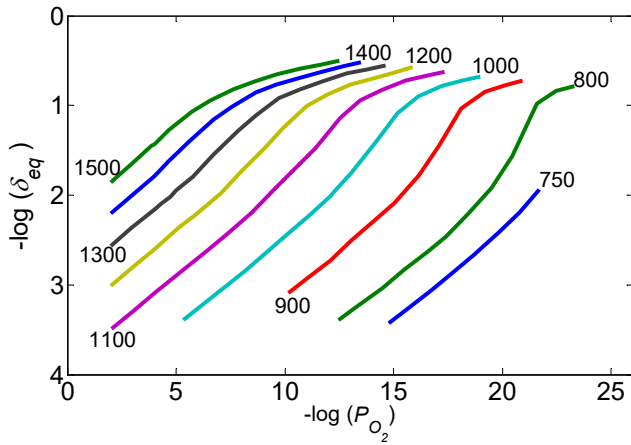

Figure 5 Equilibrium nonstoichiometry plotted against partial pressure of O_2 at different temperature in 750-1500 °C, the number close to the line represents corresponding temperature for the unit of °C .[43]

The detailed kinetics of reduction reaction using ceria as an intermediate OSM cannot be found in the literature. Thus here, it was evaluated by fitting the model to the experimental data using a tubular reactor of a packed bed of ceria particles in Chueh and Haile.[8,9] In the experiment, the ceria is heated from 800°C to 1500°C. The total gas flow rate is set as 4090 ml min^{-1} g-OSM^{-1} with the inlet pressure of O_2 of 10^{-5} atm.

Assuming the concentration of the gas in the radial direction is uniform, the concentration in the packed bed tube reactor can be described by the following equation:

$$\frac{\partial c_{i,OSM}(z,t)}{\partial t} + \frac{\partial u_{Purge}(z,t) c_{i,OSM}(z,t)}{\partial z} + D_{eff} \frac{\partial^2 c_{i,OSM}(z,t)}{\partial z^2} = -r_i(z,t) \quad (26)$$

where $i = H_2, O_2$ and $r_i(z,t)$ are given in Eq. (17) and Eq. (21), respectively.

The parameter k_{O_2} is obtained using the parameter estimation in gPROMS, which minimizes the difference between the model

prediction and the experimentally observed values in the O_2 generation rate obtained at the exit of the tubular reactor. From this minimization, k_{O_2} is estimated to be 499 kmol m^{-3} s^{-1}. Figure 6 (a) shows the comparison of O_2 generation rate at the exit of reactor from model with $k_{O_2} = 499 \, \text{kmol m}^{-2} \text{s}^{-1}$ and experimental data. With this estimation, the full model of kinetics for the reduction reaction is obtained.
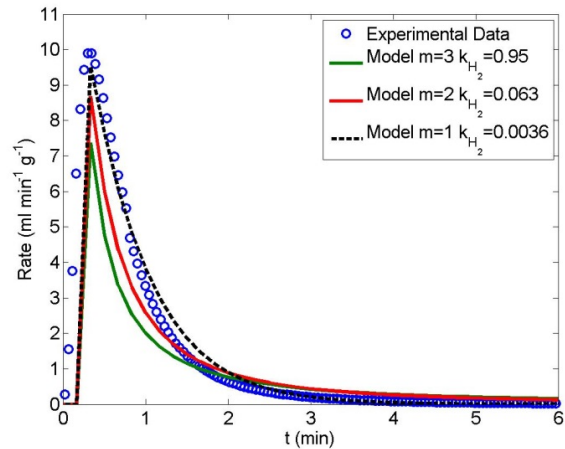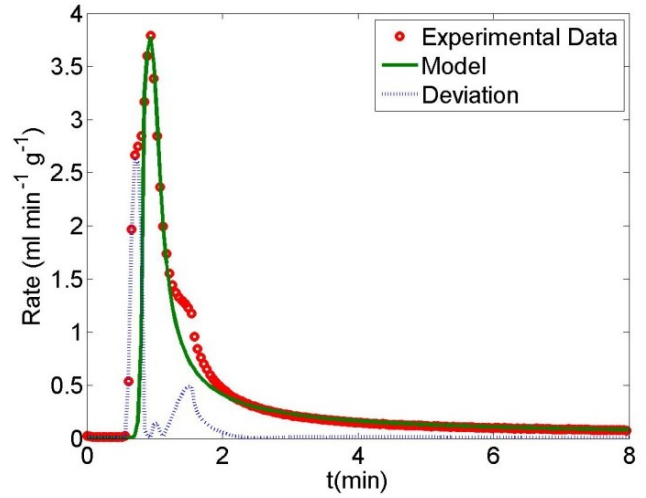

Figure 6 (a) Comparison of outlet O_2 generation rate in the reduction reaction at the exit of reactor from the model and experimental data with the estimated parameter $k_{O_2} = 499 \, \text{kmol m}^{-2} \text{s}^{-1}$. (b) Comparison of outlet H_2 generation rate in the oxidation reaction from the model and experimental data with $m = 1, 2, 3$.

In the oxidation reaction, two parameters m and k_{O_2} are needed. We fit the model equations for different values of m. With $m = 1, 2, 3$, the corresponding value of k_{H_2} is obtained by

the parameter estimation, and the comparisons are shown in Figure 6 (b). As we can see, m = 1 predicts the correct peak value, and thus it was adopted and corresponding k_{H_2} is used.

With the kinetics described by the aforementioned model, the model is complete for reactor design. Nevertheless, it is worth noting that the kinetic model is empirical, and further investigations are needed to quantify the reaction rate more rigorously.

RESULTS

Efficiency Computation

In the proposed design, a general form of the thermal efficiency $\eta_{\text{thermal-chemical}}$ is given by:

$$\eta_{\text{thermal-chemical}} = \frac{n_{H_2} HHV_{H_2}}{Q_{\text{Total}}} = \frac{n_{H_2} HHV_{H_2}}{Q_{Reheat} + Q_{Loss} + W_{Pump} + Q_{Purge} + Q_{RXN}}$$

(27)

where n_{H_2} represents the total hydrogen produced per cycle, HHV_{H_2} is the higher heating value of hydrogen, Q_{Total} is the total energy input per cycle, and W_{pump} accounts for the mechanical work input required to lower the O_2 partial pressure by the vacuum pump. Here, Q_{Reheat} accounts for the thermal energy required to heat the OSM and reactor from T_L to T_H, which is given by:

$$Q_{Reheat} = (1 - \varepsilon_S) \int_{T_L}^{T_H} \left(m_{OSM} C_P^{OSM} + m_{\text{Sup}} C_P^{\text{Sup}} \right) dT$$

(28)

where ε_S is the solid phase heat recuperation efficiency. More detailed discussions on estimating ε_S can be found from Yuan et al.[34]. In Equation (28), C_p^{OSM} and C_p^{Sup} are the specific heat of the OSM and its support, respectively. The heat loss Q_{Loss} accounts for the heat leakage from the entire reactor system:

$$Q_{Loss} = \dot{Q}_{Loss} \Delta t$$

(29)

Estimation of Q_{Loss} and $\dot{Q}_{Loss}$ can be found from Yuan et al.[34].

The heat of reaction Q_{RXN} represents the endothermic energy required to liberate oxygen during the reduction step and is given by:

$$Q_{RXN} = n_{O_2} \Delta H_{O_2}$$

(30)

The quantity Q_{Purge} accounts for the energy required to preheat the purge gas to T_L or T_H, and is given by:

$$Q_{Purge} = (1 - \varepsilon_G) \left(\int_{T_\infty}^{T_L} C_P^{\text{gas}} n_{\text{gas}}^L dT + \int_{T_\infty}^{T_H} C_P^{\text{gas}} n_{\text{gas}}^H dT \right)$$

(31)

where T_∞ is the ambient temperature, n_{gas}^L and n_{gas}^H are the total amount of purge gas used for oxidation and reduction reactions, respectively, and ε_G is the efficiency of the gas heat exchanger.

Operating Parameters and Efficiency

We simulated the reduction and oxidation reactions using the mathematical model introduced in Section 3. The two reactions are performed simultaneously in reaction chambers on opposing sides of the circle shown in Figure 2. The reactor design and operating parameters used for this simulation are listed in Table 2. The reactor was designed so that the average fuel output becomes approximately 1.0 kW with maximum efficiency. To minimize heat dissipation from the chamber surface, the surface area must be minimized, and thus a parallel array of tubes with a high surface area per unit volume should be avoided. The length-to-width ratio (L/D) of the reaction chamber is assumed to be 3.0, which is sufficiently small but still may allow us to construct a chamber that would not cause non-uniform distribution of the gas flow. Under such considerations, we used the parameters shown in Table 2. The pipe dimensions (R_{LM} and R_{Sup}) were based on low cost thin walled extruded graphite tubes that are commercially available so that the thermal mass is minimized. The number of pipes inside of a chamber is computed based on the size of chamber and size of pipes; no optimization has been done for this parameter and it is treated as a constant.

The operating parameters were also chosen carefully to maximize the efficiency. To save the energy to pump the LM, a small value was chosen for the velocity u_{LM}; the low velocity would not hinder heat transfer because of the high heat transfer coefficient h_{LM}. Operating parameters for heat recuperation such as preheating time t_{preheat}, initial chamber temperature of reduction step T_{H-} and oxidation step T_{L+} are determined by

carrying out cyclic simulation of heat transfer in an eight chamber reactor, and detailed information can be found elsewhere[34]. The duration of the remaining steps shown in Figure 3, where the purging time t_{purge} and pumping time t_{pump}, were determined such that the maximum efficiency is achieved, as discussed in Section 4.4 in detail. Influence of other critical parameters, such as the gas velocity u_{gas} and the reduction temperature T_H are also discussed in Section 4.4.

Table 2 Reactor design parameters and operating parameters

Parameters	Value	Unit	Parameters	Value	Unit
Reactor design parameters			*Oxidation reaction*		
$W_{chamber}$	0.2	m	T_L	800	°C
$H_{chamber}$	0.2	m	T_{L+}	877	°C
$L_{chamber}$	0.6	m	$u_{gas,inlet}$	0.08	m s^{-1}
η_{gas}	0.7		*OSM support properties*		
N_{pipe}	45	m	ρ_{OSM}	721.5	kg m^{-3}
R_{LM}	0.005	m	C_p^{OSM}	358	J kg^{-1} K^{-1}
R_{Sup}	0.01	m	λ_{OSM}	0.2	W m^{-1} K^{-1}
R_{OSM}	0.013	m	ε	0.6	
R_{fs}	0.0168	m	d_{32}	10.0	μm
u_{LM}	0.03	m s^{-1}	τ	1.2	
Reduction reaction			*Insulation properties*		
T_H	1500	°C	$b_{insulation}$	0.3	m
$u_{gas,inlet}$	5.0	m s^{-1}	$\lambda_{insulation}$	0.05	W m^{-1} K^{-1}
T_{H-}	1410	°C	$h_{insulation}$	5.0	W m^{-1} K^{-1}
$t_{pumping}$	0.5	min			
$t_{purging}$	7.5	min			
$t_{preheat}$	4.0	min			

Table 3 the reactor performance for eight chamber reactor system in one stage (i.e. 12 min).

Output	Value	Unit
$\eta_{thermal-chemical}$	19.8	%
n_{O_2}	1.20	mol
n_{H_2}	2.40	mol
$\bar{\delta}_{OSM}$	0.0245	
$p_{reactor}$	0.95	kW

With these parameters, the reactor performance is summarized in

Table 3. The thermal to chemical efficiency $\eta_{thermal-chemical}$ is approximately 20%. This high efficiency of our reactor gives a high overall efficiency $\eta_{solar-thermal}\eta_{thermal-chemical}$ of approximately 16%, assuming the efficiency of solar-to-thermal energy conversion $\eta_{solar-thermal}$ is 80%. This efficiency is almost one order magnitude higher than the maximum efficiency of a convectional solar thermal chemical reactor design.[12] In the next section, with the base case in

Table 3, the efficiency bottleneck is identified using a sensitivity analysis.

It should finally be noted that there still exist technical and economic uncertainties which must be considered carefully. The proposed reactor concept assumes the hot LM can be circulated between reaction chambers, which requires a thermally stable material to contain the LM. Furthermore, there may be a trade-off between the overall efficiency and capital cost. In our reactor concept where the area of the OSM in the reactor is independent of the receiver area, the amount of the OSM can be chosen independently from the solar receiver design. To quantify the cost of the OSM, an in depth technoeconomic analysis should be performed, which is beyond the scope of this work specifically.

Heat and Mass Transfer In The Chamber

Achieving fast heating is crucial to generate the vacancies in Step 1 efficiently.[7,9] Figure 7 shows the temperature profile of a chamber with the initial temperature of 1410°C after 40 seconds of heating with the LM at the temperature of 1500°C. It can be seen that the heat transfer in the radial direction of the OSM is significantly slower than that of the pipe. This is mainly due to the low thermal conductivity of the OSM, which has a porous structure that contains gas internally. Another reason is due to the endothermic reaction which results in a local cooling effect within the OSM. This effect also explains why the temperature in some parts of the OSM region becomes slightly lower than the initial temperature, 1410 °C. However, it is also apparent from Figure 7 that the OSM at bottom left are heated to the desired reaction temperature of 1500°C in a short amount of time, and the average heating rate of the OSM there can be calculated to be approximately 32°C/min. Although this heating rate is lower than that of conventional reactor designs,[7] it is sufficient for our reactor concept, because in our eight chamber design, the reaction chamber undergoing reduction only needs to be heated by 90°C (from T_{H-}=1410 °C to T_H=1500 °C) in the preheating step.
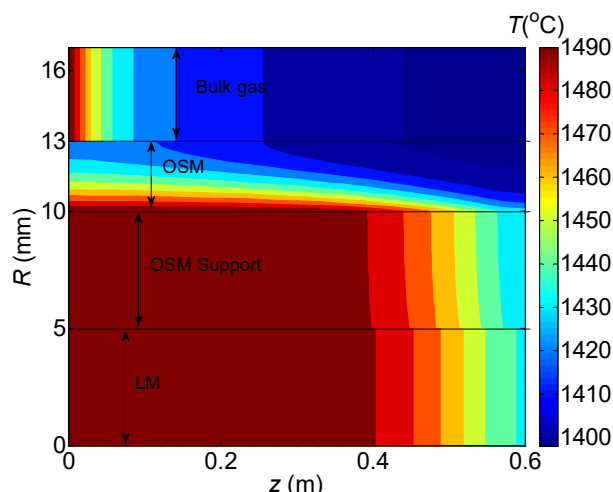
Figure 7 The temperature distribution of LM, OSM support, OSM and gas in the reduction reaction, after 40s of heating with LM at the initial temperature of 1410°C.

The heating rate of our reactor design is sufficiently fast, but the rate of oxygen removal becomes the bottleneck to improve the efficiency.[13] Figure 8 shows the axial distribution of oxygen partial pressure changes as a function of time in the bulk gas layer. As can be seen in this figure, p_{O2} increases along the axial domain, since oxygen is accumulated near the outlet of the reactor as the purge gas sweeps through the free volume in the chamber. As the reaction rate decreases with time, the amount of oxygen produced reduces, and this results in a flatter profile of p_{O2}. Nevertheless, the oxygen pressure between $z = 0.1$ and 0.6 m is still two orders of magnitude larger than the inlet partial pressure, 10^{-5}atm, and this high partial pressure of oxygen constrains the oxygen diffusion from OSM layer to the bulk gas layer.
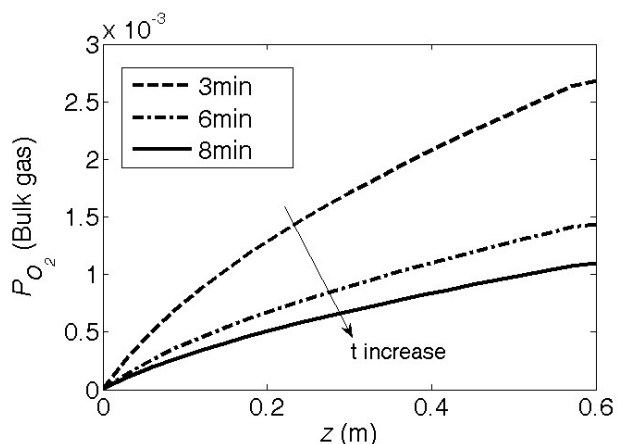

Figure 8 Distribution of oxygen partial pressure in the bulk gas along the z direction at different times during the reduction reaction.

This oxygen removal bottleneck is further investigated by analyzing the OSM layer. Figure 9 shows the distribution of

P_{O_2}, temperature T_{OSM} and nonstoichiometry δ in the OSM layer at 3 min and 8 min after the reduction step begins. At 3 min (Figure 9(a)), a large gradient in oxygen partial pressure P_{O_2} is observed in the axial direction z, while the temperature has a steep gradient in the radial direction R. Due to these spatial gradients, the nonstoichiometry δ is the lowest at the top right corner, and the highest at the bottom left corner. At 8 min (Figure 9(b)), the P_{O_2} still has a gradient in z while the temperature profile is almost uniform within the range of 4°C. Thus the nonstoichiometry (δ) distribution is almost entirely determined by P_{O_2}, which is almost uniform in the radial direction but still has a large gradient in the axial direction. This large gradient of P_{O_2} in z indicates that the factor limiting the oxygen removal is not diffusion in the OSM layer but in the bulk gas, as O_2 accumulates near the outlet of the reactor (Figure 8). This can be explained by comparing the time scale of diffusion in the radial direction R and convection in the axial direction z. The oxygen diffusion scale in radial direction R is very small for our reactor design due to the high diffusion coefficient at such high temperatures and the low total pressure of the reduction step, which is on the order of

$$t_{\text{Diffusion}} = \frac{\left(R_{\text{OSM}} - R_{\text{Sup}}\right)^2}{4D_{\text{gas}}} \sim 10^{-3}\ s\ .$$ This is significantly smaller than the characteristic time scale of convection in bulk gas which is on the order of $t_{\text{Convection}} = \dfrac{L}{u_{\text{gas}}} \sim 0.1 - 0.01s$.

Therefore, the removal of oxygen in bulk gas by the convective flow becomes a limiting factor.

There are many potential strategies to resolve the bottleneck of oxygen removal. One simple approach to facilitate the oxygen removal is to shorten the reaction chamber length at the expense of lower fuel production rate and potential maldistribution of the gas. Another option is to examine alternative electrochemical based pumping methods, which is out of scope in this study.

Parameter Sensitivity Analysis

A sensitivity analysis is performed to determine the influence of the some materials and system parameters on the reactor efficiency. To check the validity of the efficiency, the sensitivity of one of the most uncertain parameters, the reaction kinetic constant for the reduction step k_{O_2}, is investigated. The sensitivity analysis for this uncertain model parameter is crucial, since only one set of experimental data is available to fit the kinetic constant. Figure 10 shows the reactor efficiency as a

function of the kinetic constant k_{O_2}. As we can see, the efficiency is very insensitive to the value of k_{O_2} in the range of between 500 to 5000 and only results in a slight change of $\eta_{\text{thermal-chemical}}$ (< 1%) when k_{O_2} is below 500 kmol m^{-3}s^{-1}. This observation indicates that error in the value of k_{O_2}, estimated to be 499 kmol m^{-3}s^{-1} in this study, is not likely to lead to a substantial difference in the efficiency estimation. As discussed in Section 4.3, the efficiency $\eta_{\text{thermal-chemical}}$ is largely determined by the rate of oxygen removal.

Figure 10 Sensitivity of efficiency against the kinetic constant for reduction reaction, k_{O_2}.
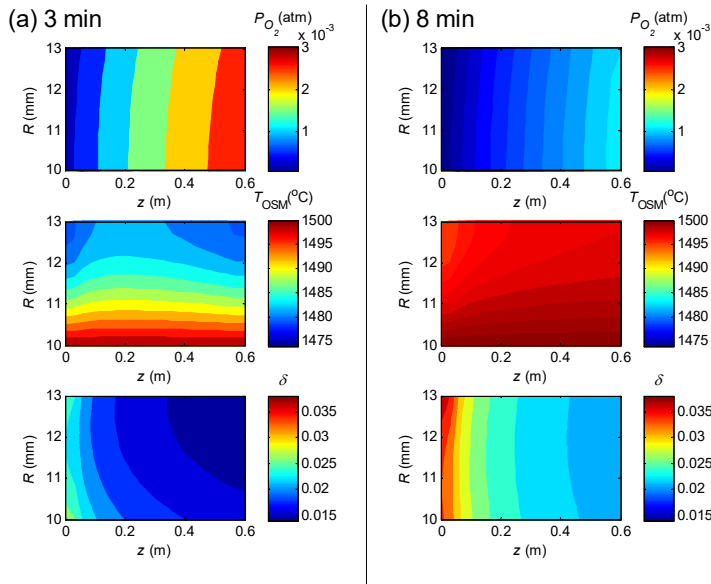

Figure 9 Distribution of partial pressure of oxygen, temperature and nonstoichiometry in OSM layer at time (a) 3 min and (b) 8 min in the reduction reaction.
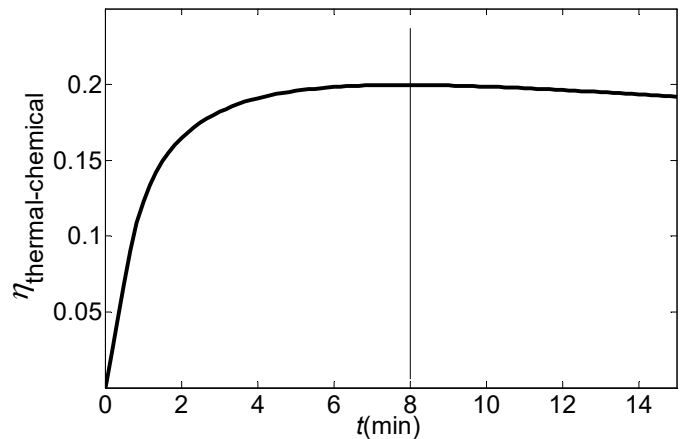
Figure 11 Efficiency against the reaction time.

The influence of the overall reaction time, which is determined by the pumping time t_{pumping} and the purging time t_{purging}, should be optimized. From Figure 11, we can determine the optimal duration of the pumping step, where all other operation parameters are fixed. In this figure, it can be seen that the efficiency reaches its maximum value at around 8.0 minutes, and decreases slightly thereafter. This is due to the trade-off between (1) increased fuel production, and (2) the preheating energy requirement for the purging gas and heat leakage through the insulated chamber surface. From this analysis, the purging time t_{purging} was determined to be 8.0 minutes.
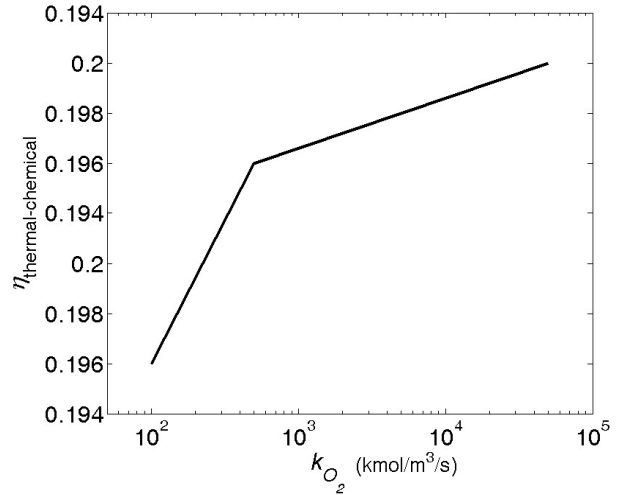
Another critical parameter that determines the efficiency is the reduction temperature of reactor which determines the extent of reduction reaction of ceria at a given pressure of oxygen. Figure 12 shows the influence of the reduction temperature T_H on the efficiency $\eta_{\text{thermal-chemical}}$ for a fixed value of the oxidation temperature T_L. As we can see from this figure, with the increase of reduction temperature, the efficiency of reactor increases almost linearly in this temperature range, despite the significant increase in the sensible heat Q_{Reheat}. This is because of the efficient heat recuperation enabled by the proposed reactor concept. However, employing a higher temperature becomes unrealistic when one considers the constraints on concentrating the sunlight[44,45], as well as materials constraints associated with the pumps, valves and piping for the fluids.
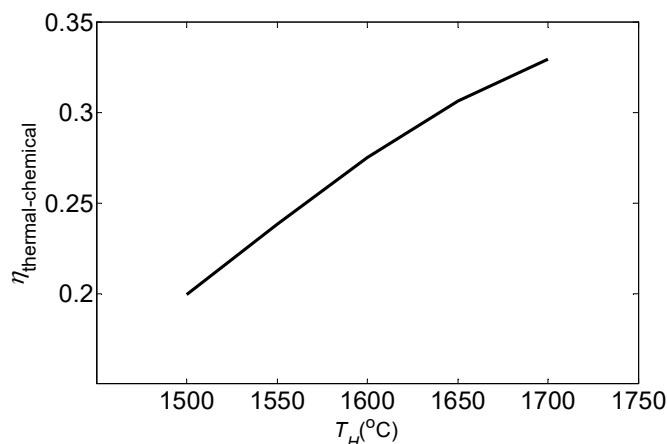
Figure 12 Reactor efficiency versus operating temperature in reduction step.
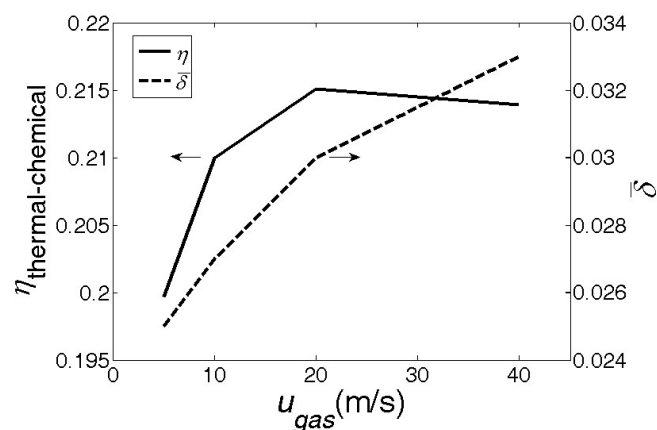

Figure 13 Reactor efficiency and average nonstoichiometry versus bulk gas purging velocity.

Another important parameter that affects the efficiency is the gas velocity of the purging gas, which determines how fast oxygen can be removed. As discussed previously, in our reactor design, the oxygen removal occurs in two directions: one is the radial direction, which is mainly determined by the oxygen diffusion in the OSM layer, and the other in the axial direction, which is determined by the bulk gas convection and is influenced significantly by the purging gas velocity. Figure 13 shows how the reactor efficiency and the average nonstoichiometry over a stage, as the purging gas velocity of bulk layer (u_{gas}) increases. Here, the average nonstoichiometry $\overline{\delta}$ is defined as:

$$\overline{\delta} = \frac{\int_{0}^{L_{chamber}} \int_{R_{Sup}}^{R_{OSM}} \delta(R, t_{preheat} + t_{pumping} + t_{purging}, z) dRdz}{\pi \left(R_{OSM}^2 - R_{Sup}^2 \right) L_{chamber}}$$

(32)

In this figure, $\overline{\delta}$ always increases for a larger value of the bulk gas velocity, which confirms that removal of oxygen from the bulk gas is a limiting factor. However, this is not the case for the reactor efficiency, $\eta_{thermal-chemical}$ which remains nearly constant when u_{gas} is over 20 m/s. This is because a larger consumption rate of the purge gas requires more preheating energy for the purge gas.

CONCLUSION

A mathematical model is developed to describe a new solar thermal chemical reactor using an LM as a heat transfer fluid. Reaction kinetic models for both reduction and oxidation are obtained by fitting to experimental data. The transient model includes the heat, mass transfer and reaction kinetics which allows us to analyze the efficiency of the new reactor concept and to investigate limiting factors. The reactor can achieve the thermal to chemical efficiency of approximately 20%, and the overall efficiency of approximately 16% under some assumptions, which is nearly one order of magnitude higher than reported values in the literature.

In our reactor design, by employing the LM as a heat transfer fluid, the heat of reaction is supplied efficiently while carrying out sensible heat recuperation simultaneously. However, removal of produced oxygen becomes the bottleneck. A sensitivity analysis is carried out to analyze the effect of some parameters. The most effective way to increase the efficiency is to increase the operating temperature. However, a higher temperatures pose other implementation challenges. The trade-off between the efficiency and capital cost should be investigated carefully. Nevertheless, to our knowledge the reactor concept presented herein is the first two-step metal oxide reactor to indicate that efficiencies as high as 20% are obtainable by using a full transient model including the reaction kinetics. Thus, the reactor concept presented herein offers an interesting pathway to high efficiency solar fuels reactors.

NOMENCLATURE

Abbreviations

LM	Liquid metal
OSM	Oxygen storage material

Dimensions

R	Radial position

t	Time
z	Axial position

Super- and subscripts

Convection	Convection
Diffusion	Diffusion
eq	Equilibrium
gas	Bulk gas
fs	Free space
H_2	Hydrogen
inlet	inlet
preheat	Preheating step
pumping	Pumping step
purging	Purging step
thermal-chemical	Thermal to chemical energy conversion
O_2	Oxygen
solar-thermal	Solar to thermal energy conversion
solar-chemical	Solar to chemical energy conversion
H	High temperature (reduction reaction)
L	Low temperature (oxidation reaction)
LM	Liquid metal
OSM	Oxygen storage material
Sup	OSM support

Symbols

A	Surface area normalized by volume
$b_{insulation}$	Thickness of insulation
C	Concentration profile
C_p	Heat capacity
d_{32}	OSM pore scale particle size
d	Diameter
D_{eff}	Effective diffusion coefficient in OSM layer
Gz_H	Graetz number
h	Heat transfer coefficient
$H_{chamber}$	Height of chambers
HHV_{H_2}	Higher heating value of H_2
k_{gas}	Mass transfer coefficient
k	Reaction kinetic constant
K_{KV}	Equilibrium constant
$L_{chamber}$	Length of chambers
n_{gas}	Total purge gas used
n	Total number of moles of gas produced in a stage by a chamber

N_{pipe}	Number of pipes inside of one chamber
p_{O_2}	Partial pressure of oxygen
$p_{reactor}$	Reactor power
Q	Heat input
r_i	Reaction rate
R	Radius of pipe
Sc_{gas}	Schmidt number
T	Temperature profile
T_{H-}	Initial Chamber temperature of reduction step
T_{L+}	Initial Chamber temperature of oxidation step
T_{pump}	Pump temperature
T_∞	Environmental temperature
u	Velocity
$W_{chamber}$	Width of chamber
ΔH_{O_2}	Heat of reaction of reduction reaction
δ	Nonstoichiometry
$\overline{\delta}_{OSM}$	Average nonstoichiometry reached in OSM at end of stage
λ	Thermal conductivity
ρ	Density
ε	Porosity of OSM
ε_G	Gas-gas heat exchanger efficiency
ε_S	Sensible heat recuperation efficiency
η	Energy conversion efficiency

REFERENCES

(1) Funk, J. E.; Reinstrom, R. M. Energy Requirements in the Production of Hydrogen from Water. Ind. Eng. Chem. Process Des. Dev. 1966, 5, 336.

(2) Nakamura, T. Hydrogen Production from Water Utilizing Solar Heat at High Temperatures. Sol. Energy 1977, 19, 467.

(3) Steinfeld, A.; Frei, A.; Kuhn, P.; Wuillemin, D. Solar Thermal Production of Zinc and Syngas via Combined ZnO-Reduction and CH 4-Reforming Processes. Int. J. Hydrogen Energy 1995, 20, 793.

(4) Funk, J. E. Thermochemical Hydrogen Production: Past and Present. Int. J. Hydrogen Energy 2001, 26, 185.

(5) Steinfeld, A. Solar Thermochemical Production of Hydrogen—a Review. Sol. Energy 2005, 78, 603.

(6) Zinkevich, M.; Djurovic, D.; Aldinger, F. Thermodynamic Modelling of the Cerium–oxygen System. Solid State Ionics 2006, 177, 989.

(7) Chueh, W. C.; Falter, C.; Abbott, M.; Scipio, D.; Furler, P.; Haile, S. M.; Steinfeld, A. High-Flux Solar-Driven Thermochemical Dissociation of CO2 and H2O Using Nonstoichiometric Ceria. Science 2010, 330, 1797.

(8) Chueh, W. C.; Haile, S. M. Ceria as a Thermochemical Reaction Medium for Selectively Generating Syngas or Methane from H2O and CO2. ChemSusChem 2009, 2, 735.

(9) Chueh, W. C.; Haile, S. M. A Thermochemical Study of Ceria: Exploiting an Old Material for New Modes of Energy Conversion and CO2 Mitigation. Philos. Trans. A. Math. Phys. Eng. Sci. 2010, 368, 3269.

(10) Diver, R. B.; Miller, J. E.; Allendorf, M. D.; Siegel, N. P.; Hogan, R. E. Solar Thermochemical Water-Splitting Ferrite-Cycle Heat Engines. J. Sol. Energy Eng. 2008, 130, 041001.

(11) Ermanoski, I.; Siegel, N. P.; Stechel, E. B. A New Reactor Concept for Efficient Solar-Thermochemical Fuel Production. J. Sol. Energy Eng. 2013, 135, 031002.

(12) Furler, P.; Scheffe, J.; Gorbar, M.; Moes, L. Solar Thermochemical CO2 Splitting Utilizing a Reticulated Porous Ceria Redox System. Energy & Fuels 2012, 26, 7051.

(13) Keene, D. J.; Davidson, J. H.; Lipiński, W. A Model of Transient Heat and Mass Transfer in a Heterogeneous Medium of Ceria Undergoing Nonstoichiometric Reduction. J. Heat Transfer 2013, 135, 052701.

(14) Lapp, J.; Davidson, J. H.; Lipiński, W. Efficiency of Two-Step Solar Thermochemical Non-Stoichiometric Redox Cycles with Heat Recovery. Energy 2012, 37, 591.

(15) Lapp, J.; Davidson, J. H.; Lipiński, W. Heat Transfer Analysis of a Solid-Solid Heat Recuperation System for Solar-Driven Nonstoichiometric Redox Cycles. J. Sol. Energy Eng. 2013, 135, 031004.

(16) Lapp, J.; Lipiński, W. Transient Three-Dimensional Heat Transfer Model of a Solar Thermochemical Reactor for H 2 O and CO 2 Splitting Via Nonstoichiometric Ceria Redox Cycling. J. Sol. Energy Eng. 2014, 136, 031006.

(17) Loutzenhiser, P. G.; Meier, A.; Steinfeld, A. Review of the Two-Step H2O/CO2-Splitting Solar Thermochemical Cycle Based on Zn/ZnO Redox Reactions. Materials (Basel). 2010, 3, 4922.

(18) Lipiński, W.; Davidson, J. H.; Haussener, S.; Klausner, J. F.; Mehdizadeh, a. M.; Petrasch, J.; Steinfeld, a.; Venstrom, L. Review of Heat Transfer Research for Solar Thermochemical Applications. J. Therm. Sci. Eng. Appl. 2013, 5, 021005.

(19) Miller, J. E.; Allendorf, M. A.; Ambrosini, A.; Coker, E. N.; Diver, R. B.; Ermanoski, I.; Evans, L. R.; Hogan, R. E.; Mcdaniel, A. H. Development and Assessment of Solar-Thermal-Activated Fuel Production: Phase 1 Summary; 2012.

(20) Muhich, C. L.; Evanko, B. W.; Weston, K. C.; Lichty, P.; Liang, X.; Martinek, J.; Musgrave, C. B.; Weimer, A.

W. Efficient Generation of H2 by Splitting Water with an Isothermal Redox Cycle. Science 2013, 341, 540.

(21) Siegel, N. P.; Miller, J. E.; Ermanoski, I.; Diver, R. B.; Stechel, E. B. Factors Affecting the Efficiency of Solar Driven Metal Oxide Thermochemical Cycles. Ind. Eng. Chem. Res. 2013, 52, 3276.

(22) Steinfeld, A.; Sanders, S.; Palumbo, R. Design Aspects of Solar Thermochemical Engineering—a Case Study: Two-Step Water-Splitting Cycle Using the Fe3O 4/FeO Redox System. Sol. Energy 1999, 65, 43.

(23) Wei, B.; Saadatfar, B.; Fakhrai, R.; Fransson, T. Review on the Two-Step-Conversion of CO2 Driven by Solar Energy. J. MacroTrends Energy Sustain. 2013, 1, 139.

(24) Xu, R.; Wiesner, T. F. Dynamic Model of a Solar Thermochemical Water-Splitting Reactor with Integrated Energy Collection and Storage. Int. J. Hydrogen Energy 2012, 37, 2210.

(25) Scheffe, J. R.; Steinfeld, A. Oxygen Exchange Materials for Solar Thermochemical Splitting of H2O and CO2: A Review. Mater. Today 2014, 17, 341.

(26) Perkins, C, Lichty P., W. W. Thermal ZnO Dissociation in a Rapid Aerosol Reactor as Part of a Solar Hydrogen Production Cycle. Int. J. Hydrogen Energy 2008, 33, 499.

(27) Roeb, M.; Säck, J.-P.; Rietbrock, P.; Prahl, C.; Schreiber, H.; Neises, M.; de Oliveira, L.; Graf, D.; Ebert, M.; Reinalter, W.; et al. Test Operation of a 100kW Pilot Plant for Solar Hydrogen Production from Water on a Solar Tower. Sol. Energy 2011, 85, 634.

(28) Kaneko, H.; Miura, T.; Fuse, A.; Ishihara, H.; Taku, S.; Fukuzumi, H.; Naganuma, Y.; Tamaura, Y. Rotary-Type Solar Reactor for Solar Hydrogen Production with Two-Step Water Splitting Process. 2007, 78, 2287.

(29) Gokon, N.; Takahashi, S.; Yamamoto, H.; Kodama, T. Thermochemical Two-Step Water-Splitting Reactor with Internally Circulating Fluidized Bed for Thermal Reduction of Ferrite Particles. Int. J. Hydrogen Energy 2008, 33, 2189.

(30) Scheffe, J.; Welte, M.; Steinfeld, A. Reduction of Cerium Dioxide in an Aerosol Tubular Reactor for the Thermal Dissociation of CO 2 and H 2 O Two-Step Solar Thermochemical Cycle. Ind. Eng. Chem. Res. 2014, 53, 2175.

(31) Koepf, E.; Advani, S. G.; Steinfeld, A.; Prasad, A. K. A Novel Beam-Down, Gravity-Fed, Solar Thermochemical Receiver/reactor for Direct Solid Particle Decomposition: Design, Modeling, and Experimentation. Int. J. Hydrogen Energy 2012, 37, 16871.

(32) Kim, J.; Henao, C. A.; Johnson, T. A.; Dedrick, D. E.; Miller, J. E.; Stechel, E. B.; Maravelias, C. T. Methanol Production from CO2 Using Solar-Thermal Energy: Process Development and Techno-Economic Analysis. Energy Environ. Sci. 2011, 4, 3122.

(33) Lange, M.; Roeb, M.; Sattler, C.; Pitz-Paal, R. T–S Diagram Efficiency Analysis of Two-Step

Thermochemical Cycles for Solar Water Splitting under Various Process Conditions. Energy 2014, 67, 298.

(34)   Yuan, C.; Jarrett, C.; Chueh, W.; Kawajiri, Y.; Henry, A. A New Solar Fuels Reactor Concept Based on a Liquid Metal Heat Transfer Fluid: Reactor Design and Efficiency Estimation. Sol. Energy, submitted (Available as Supporting Information for Review Only for this manuscript).

(35)   DeAngelis, A.; Henry, A. Sensitivity Analysis of a High Temperature Liquid Metal Based Solar Receiver. In Proceedings of the 11th AIAA/ASME Joint Thermophysics and heat Transfer Conference; 2014.

(36)   Rezaei, F.; Subramanian, S.; Kalyanaraman, J.; Lively, R. P.; Kawajiri, Y.; Realff, M. J. Modeling of Rapid Temperature Swing Adsorption Using Hollow Fiber Sorbents. Chem. Eng. Sci. 2014, 113, 62.

(37)   Luo, L.; Tondeur, D. Optimal Distribution of Viscous Dissipation in a Multi-Scale Branched Fluid Distributor. Int. J. Therm. Sci. 2005, 44, 1131.

(38)   Poling, B.; Prausnitz, J.; Paul, O. J. The Properties of Gases and Liquids; 2000.

(39)   Incropera, F. P.; Lavine, A. S.; DeWitt, D. P. Fundamentals of Heat and Mass Transfer; John Wiley & Sons, 2011.

(40)   Sharafat, S.; Ghoniem, N. Summary of Thermo-Physical Properties of Sn , Comparison of Properties of Sn , Sn-Li , Li , and Pb-Li. UCLA-UCMEP-00-31 Rep. 2000, 1.

(41)   McCabe, W. L.; Smith, J. C.; Harriott, P. Unit Operations of Chemical Engineering, 7th ed.; McGraw-Hill New York, 2004.

(42)   Santos, H.; Costa, M. Analysis of the Mass Transfer Controlled Regime in Automotive Catalytic Converters. Int. J. Heat Mass Transf. 2008, 51, 41.

(43)   Panlener, R. J.; Blumenthal, R. N. A Thermodynamic Study of Nonstoichiometric Cerium Dioxide. J. Phys. Chem. Solids 1975, 36, 1213.

(44)   Fend, T.; Hoffschmidt, B.; Pitz-Paal, R.; Reutter, O.; Rietbrock, P. Porous Materials as Open Volumetric Solar Receivers: Experimental Determination of Thermophysical and Heat Transfer Properties. Energy 2004, 29, 823.

(45)   Fend, T.; Pitz-Paal, R.; Reutter, O.; Bauer, J. Ö.; Hoffschmidt, B. Two Novel High-Porosity Materials as Volumetric Receivers for Concentrated Solar Radiation. Sol. Energy Mater. Sol. Cells 2004, 84, 291.